Supporting Information

Enhancing Li⁺ transport efficiency in solid-state Li-ion batteries with ceramic-array-based composite electrolyte

Shu-Ming Yeh and Chia-Chen Li*

Department of Materials Science and Engineering, National Tsing Hua University, Hsinchu 30013, Taiwan

*Corresponding author. Tel.: 886-3-5715131. E-mail: cc.li@mx.nthu.edu.tw
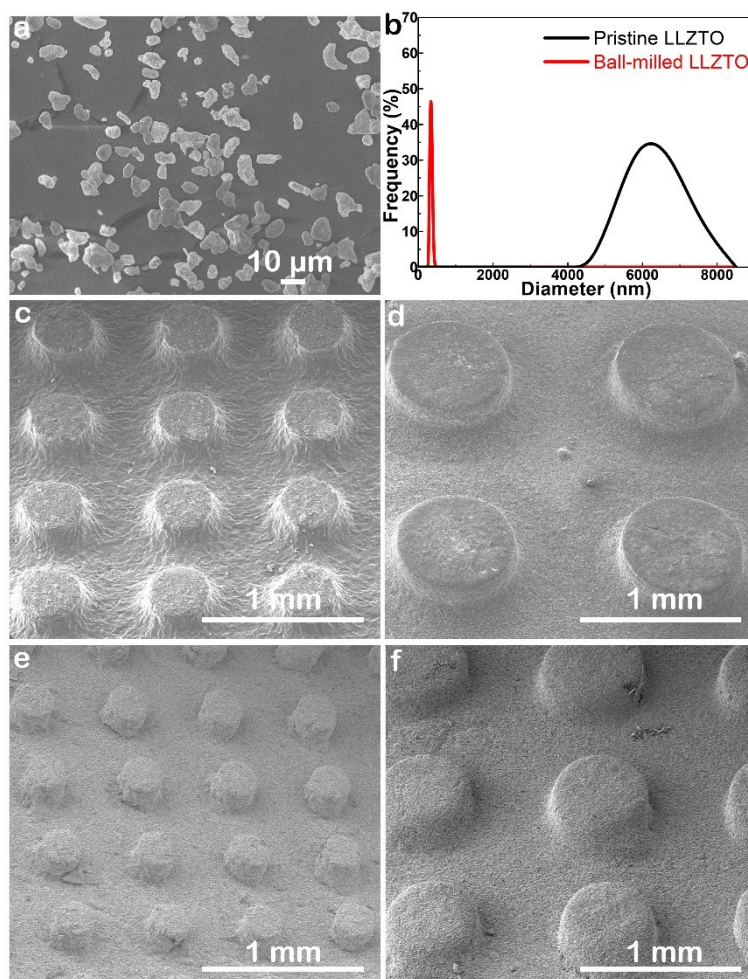
1. Supplementary data

Figure S1 SEM images of (a) as-received LLZTO particles, ceramic green bodies of LLZTO arrays with pillar diameters of (c) 315 μm and (d) 700 μm, and sintered LLZTO arrays with pillar diameters of (e) 250 μm and (f) 550 μm. (b) Particle size distributions of the as-received and milled LLZTO powders.

Figure S1a displays the as-received LLZTO particles, which have a micron size. These particles can be wet-milled to achieve a uniform size with a median diameter of 340 nm, making them suitable for fabricating the LLZTO array.

The pillar size in the array is solely determined by the resolution of the 3D printer, which is 50 μm. Figure S1c and S1d displays the molded LLZTO arrays with different pillar diameters. Noticeable shrinkage is observed upon sintering at 1150 °C for 6 h, as depicted in Figure S1e and S1f.
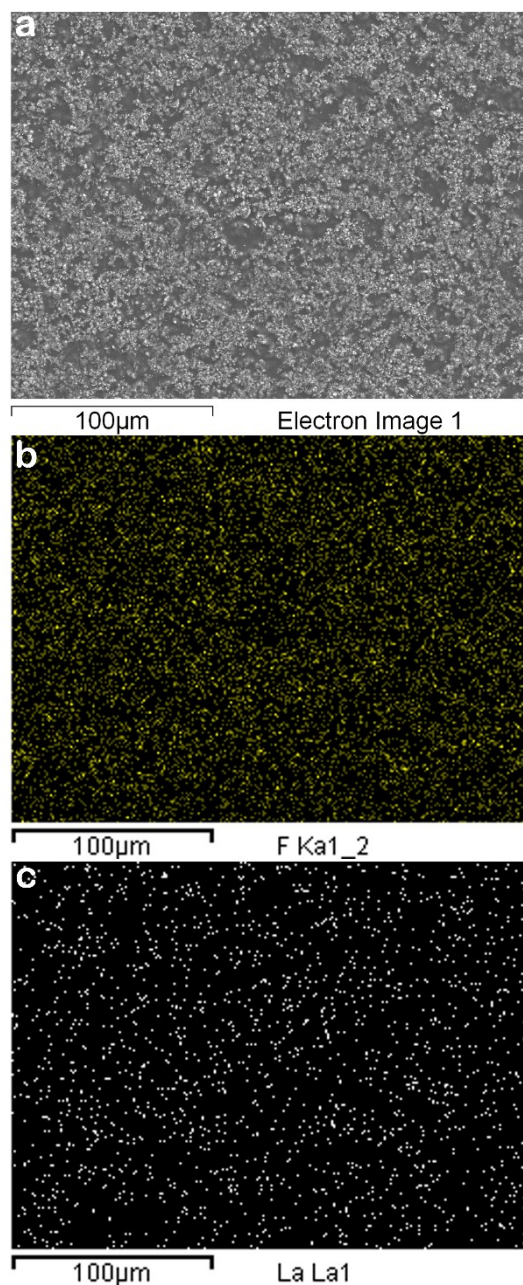
Figure S2 (a) SEM image and the corresponding elemental mappings of (b) F and (c) La for the dispersion-CSE.

This data in Figure S2 provides clear evidence of the homogeneous distribution of PVDF-HFP and LLZTO within the dispersion-CSE.
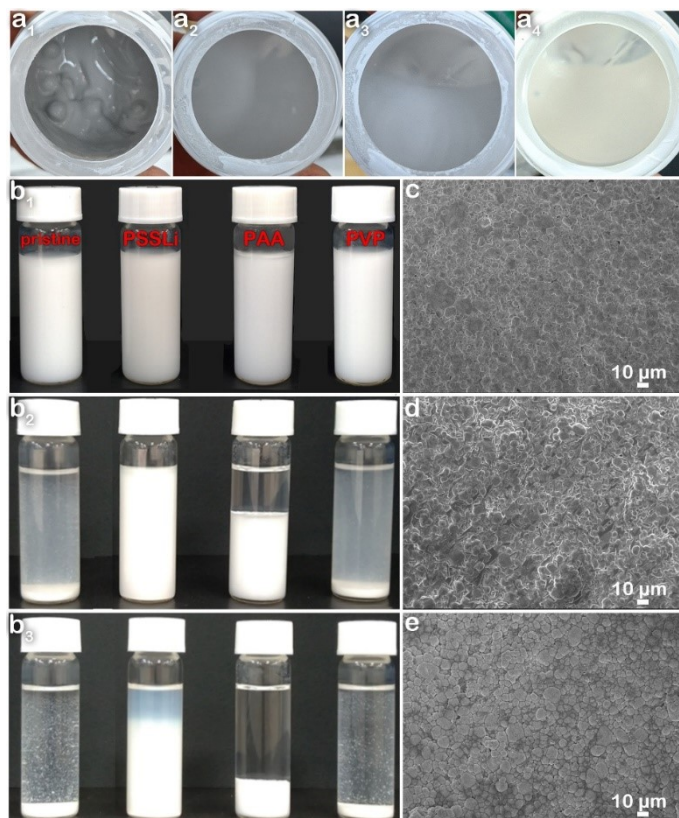
Figure S3 Photos showcasing LLZTO slurries with varying [PSSLi]: (a_1) 0 wt%, (a_2) 2 wt%, (a_3) 3 wt%, and (a_4) 5 wt%. Additional photos illustrating 1 wt% LLZTO powder suspended in ethanol with and without 10 wt% of the dispersant, PSSLi, PAA, or PVP, and subject to sedimentation tests for (b_1) 0 min, (b_2) 1 h, and (b_3) 72 h. Micrographs displaying sintered ceramic bodies of LLZTO derived from slurries containing (c) 2 wt%, (d) 3 wt%, and (e) 5 wt% [PSSLi].

Based on the findings in Figure S2a_1-a_4, it is evident that achieving good flowability in the LLZTO slurry requires a critical concentration of 5 wt% [PSSLi] (Figure S2a_4). Furthermore, the comparative analysis in Figure S2b_1-b_3 reveals that only the addition of PSSLi effectively retards the rapid sedimentation of the LLZTO powder in the suspension, indicating the superior dispersion efficiency of PSSLi.

The relative density of the sintered LLZTO ceramic bodies, derived from slurries containing 2, 3, and 5 wt% [PSSLi], was 86.0%, 90.3%, and 96.3%, respectively. The corresponding SEM images are shown in Figure S2c-e.
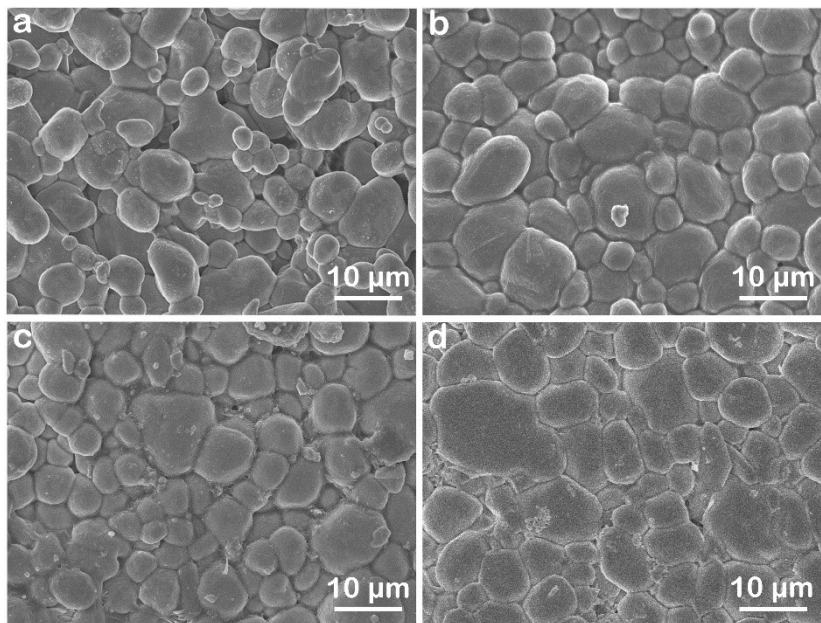
Figure S4 Micrographs displaying ceramic bodies of LLZTO, prepared with the slurry containing 5 wt% [PSSLi], after sintering at 1150 °C for (a) 3h, (b) 4 h, (c) 5h, and (d) 6 h.

The relative densities of the samples in Figure S3a, S3b, S3c, and S3d are 87.1%, 94.4%, 95.1%, and 96.3%, respectively.
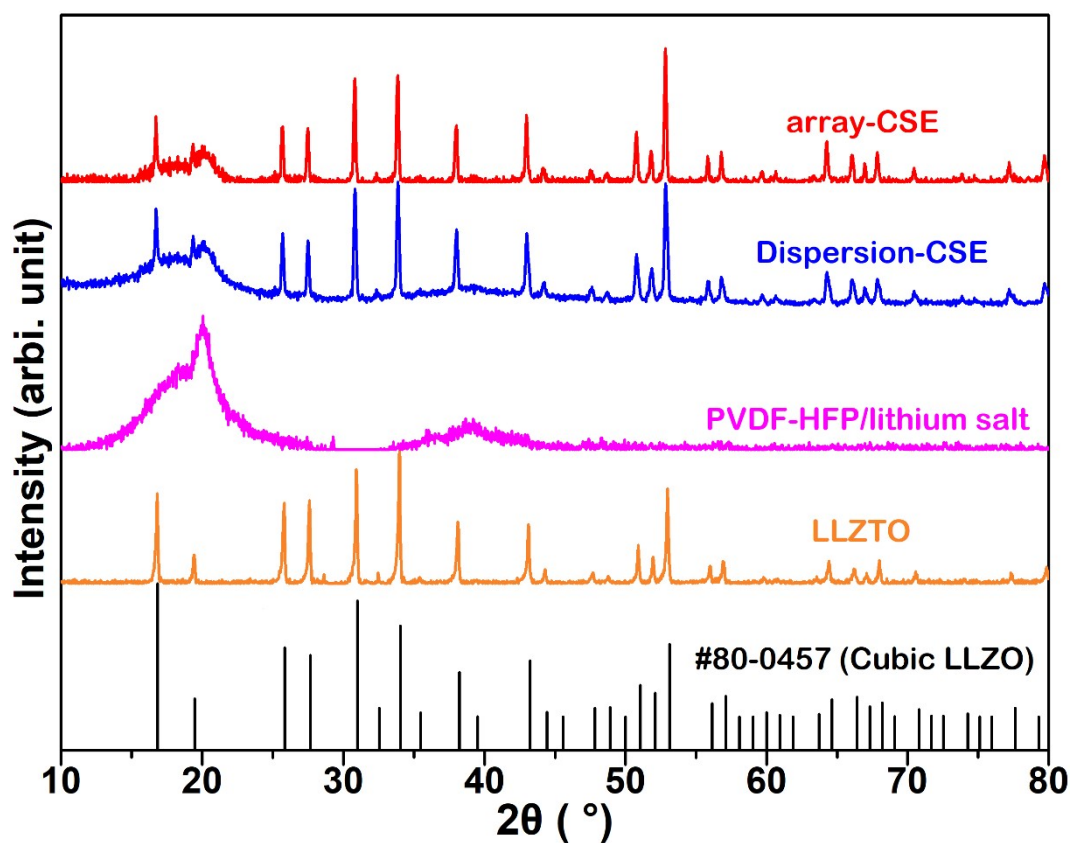
Figure S5 XRD spectra of the array-CSE, dispersion-CSE, as-received LLZTO powder, and PDVF-HFP with 10% lithium salt.

Figure S5 clearly demonstrates that the LLZTO crystalline structure remains in its original cubic phase after mixing with PVDF-HFP and lithium salt in the CSE.
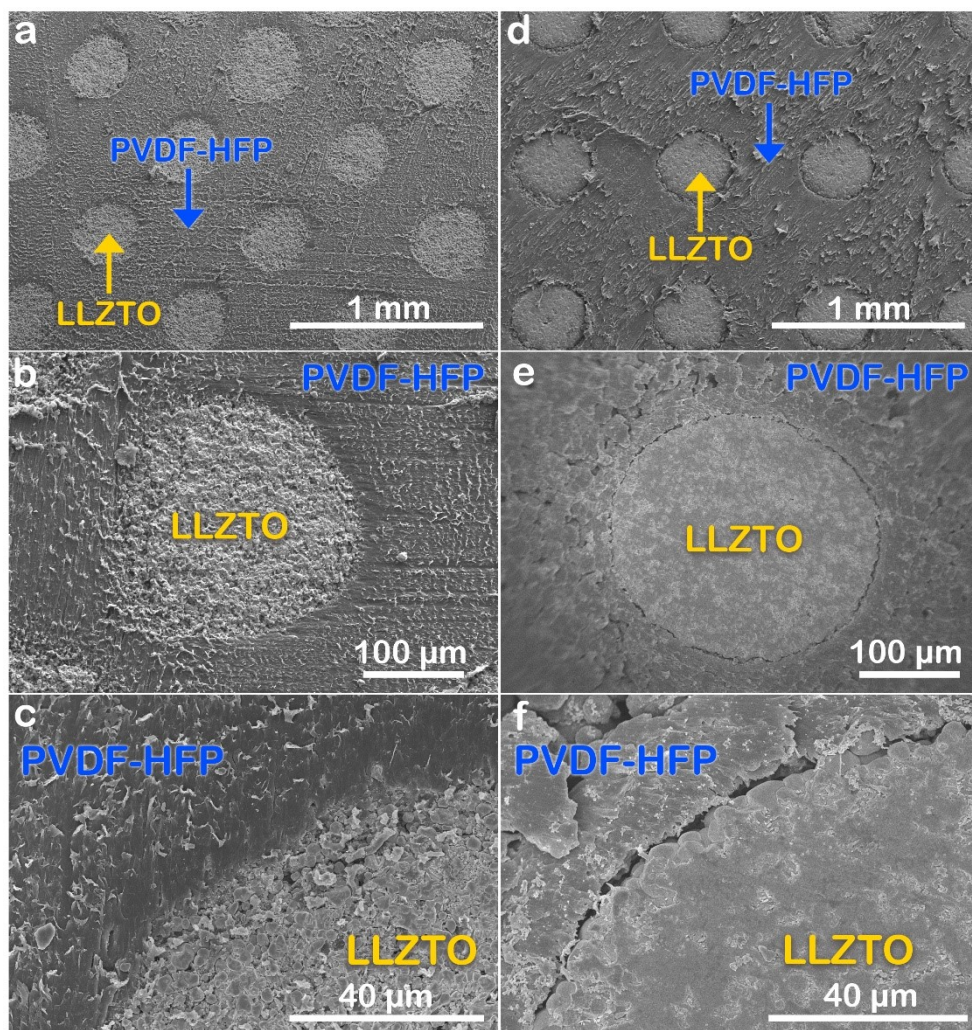
Figure S6 SEM images of array-CSEs prepared (a-c) with and (d-f) without the addition of a coupling agent KH560, shown at different magnifications.
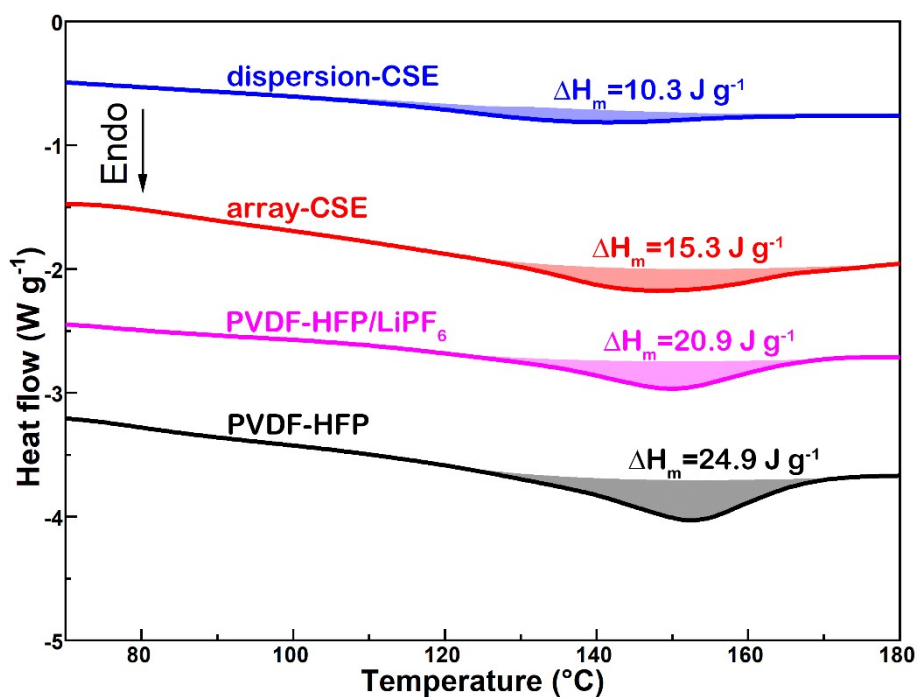
Figure S7 DSC results of PVDF-HFP, a mixture of PVDF-HFP with 10 wt% LiPF$_6$, array-CSE, and dispersion-CSE. The array-CSE and dispersion-CSE are composed of 70 wt% LLZTO and 30 wt% PVDF-HFP, wherein PVDF-HFP contains an additional 10 wt% LiPF$_6$ (based on PVDF-HFP mass).

Based on the melting heat ($\Delta H_{m,ref}$ = 104.7 J g^{-1}) of a 100% crystalline PVDF-HFP and Eq. (S1),[S1] the crystallinity (X_c) of PVDF-HFP can be determined accordingly:

$$X_c(\%) = \frac{\Delta H_m}{\Delta H_{m,ref}} \times 100\%$$

(S1)

The pure PVDF-HFP, mixture of PVDF-HFP with 10 wt% LiPF$_6$, array-CSE, and dispersion-CSE each exhibit an endothermic peak with heats of 24.9, 20.9, 15.3, and 10.3 J g^{-1}, respectively, at their melting points (~140-150 °C). Consequently, the calculated X_c of PVDF-HFP in the above samples is 24%, 20%, 15%, and 10%, respectively.

Supplementary reference:

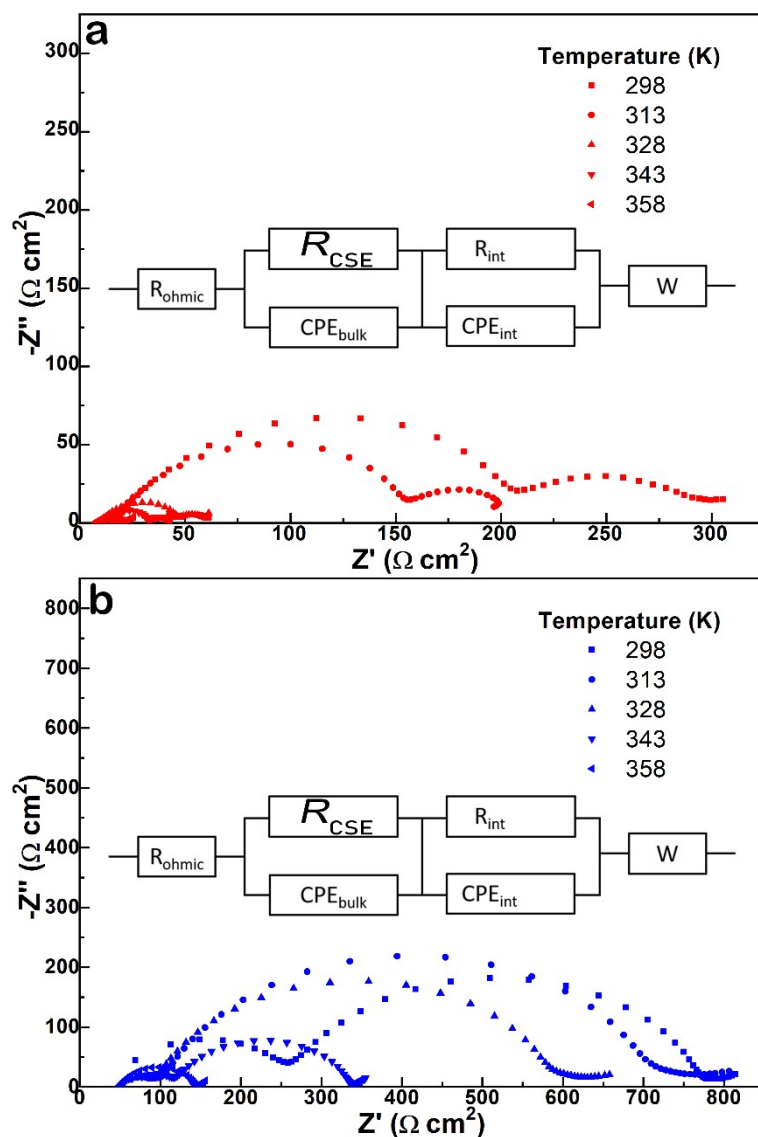[S1] J.H. Cao, B.K. Zhu, Y.Y. Xu, *J. Membr. Sci.* 28 (2006) 446-453.

Figure S8 Nyquist impedance spectra of the Li│CSE│Li cells assembled with (a) array-CSE and (b) dispersion-CSE measured at temperatures ranging from 298 to 358K.

Table S1 Bulk resistance (R_{CSE} in Ω cm^2) of Li│CSE│Li cells assembled with array-CSE and dispersion-CSE at different temperatures.

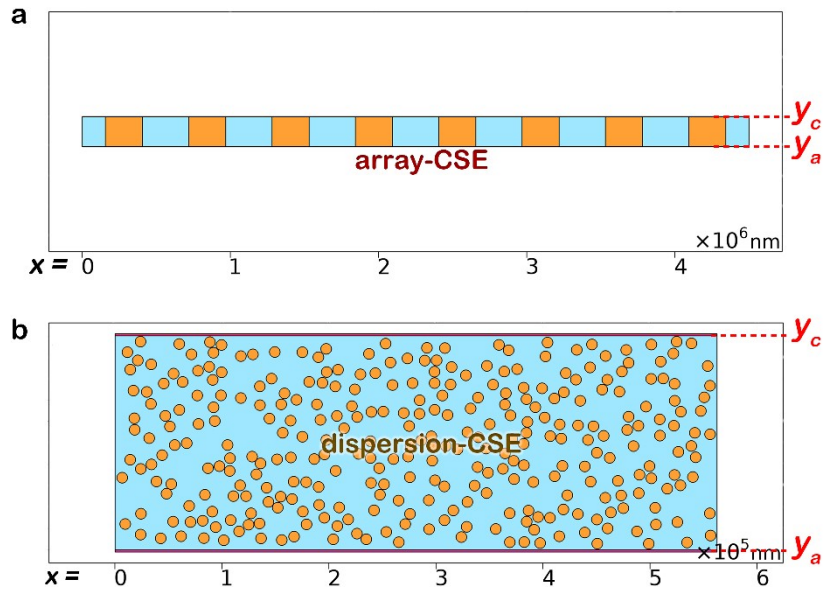| T (K)	array-CSE	dispersion-CSE
298	192.4	253.2
313	117.5	140.4
328	36.5	68.6
343	22.6	42.9
358	15.4	28.0

Figure S9 2D computational models of (a) array-CSE and (b) dispersion-CSE designed for numerical FEM simulations.

Table S2 Parameters used for numerical FEM simulations.

Parameter	Units	Value	Description
$D_{Li^+}^{c}$	m^2 s^{-1}	7.5×10^{-12}	Li$^+$ diffusivity in LLZTO
$D_{Li^+}^{p}$	m^2 s^{-1}	1.0×10^{-13}	Li$^+$ diffusivity in PVDF-HFP
$D_{Li^+}^{i}$	m^2 s^{-1}	10^{-9}, 10^{-12}, or 10^{-15}	Li$^+$ diffusivity in interface layer
$D_{Li^+}^{LFP}$	m^2 s^{-1}	$> 10^{-9}$	Li$^+$ diffusivity in LFP cathode
$D_{Li^+}^{Li}$	m^2 s^{-1}	$> 10^{-9}$	Li$^+$ diffusivity in Li anode
Mc	wt%	70	mass ratio of LLZTO in a CSE
Mp	wt%	30	mass ratio of PVDF-HFP in a CSE
W_{CSE}	μm	4.5 mm/562.5 μm	width of a CSE
t_{CSE}	μm	200	thickness of a CSE
l	nm	1 or 10	interface layer thickness
T	ºC	298.15	charge-discharge temperature
t	s	18,000	time for discharge at 1C

Numerical simulations using the Nernst-Plank equation calculation module in the COMSOL Multiphysics finite element software were employed to investigate the Li$^+$ flux and transport trajectory

within the CSEs of LFP│CSE│Li cells. Two distinct 2D models were created to represent the array-CSE and dispersion-CSE, as depicted in Figure S7. The array-CSE consisted of LLZTO pillars with a diameter of 250 μm embedded in a PVDF-HFP matrix, while the dispersion-CSE comprised dispersed LLZTO spherical particles with a diameter of 10 μm in the same matrix. Notably, these simulations were conducted under the assumption that no electrochemical reactions occur within the CSEs. Essential parameters required for the calculations are listed in Table S2.

The transport of Li$^+$ ions within the CSEs was effectively described by a simplified Nernst-Plank equation, as shown in Eq. (S1), considering diffusion and migration under an electric field. The diffusivity (D_{Li}) and concentration (c_{Li}) of the mobile Li$^+$ ions played key roles in determining the Li$^+$ flux (J_{Li}). The mobility of Li$^+$ ions ($u_{m,Li}$) was associated with D_{Li} through Eq. (S2). To ensure electrical neutrality within the CSEs, the calculations adhered to the electroneutrality condition as expressed by Eq. (S3).

$$J_{Li} = -D_{Li}\nabla c_{Li} - z_{Li}u_{m,Li}Fc_{Li}\nabla V \tag{S1}$$

$$u_{m,Li} = \frac{D_{Li}}{RT} \tag{S2}$$

$$\sum z_i c_i = 0 \tag{S3}$$

For the simulations, c_{Li} was maintained as a constant 1 mol m^{-3}. At the boundaries of the CSEs, where x < 0 and > 4.5 mm for the array-CSE, and x < 0 and > 562.5 μm for the dispersion-CSE, c_{Li} and J_{Li} were both set to 0. During the charge and discharge processes, c_{Li} was kept equivalent to the concentration of uncompensated negative charge (c_n) in the electrolyte. Moreover, the potential voltage difference between the Li anode and LFP cathode was varied between 2.5 and 4.2 V. During discharge, an open boundary condition was implemented at specific locations (y_a and y_c), as illustrated in Figure S7, to ensure a complete outflow of Li$^+$ ions from the electrode, thereby preventing ion accumulation.
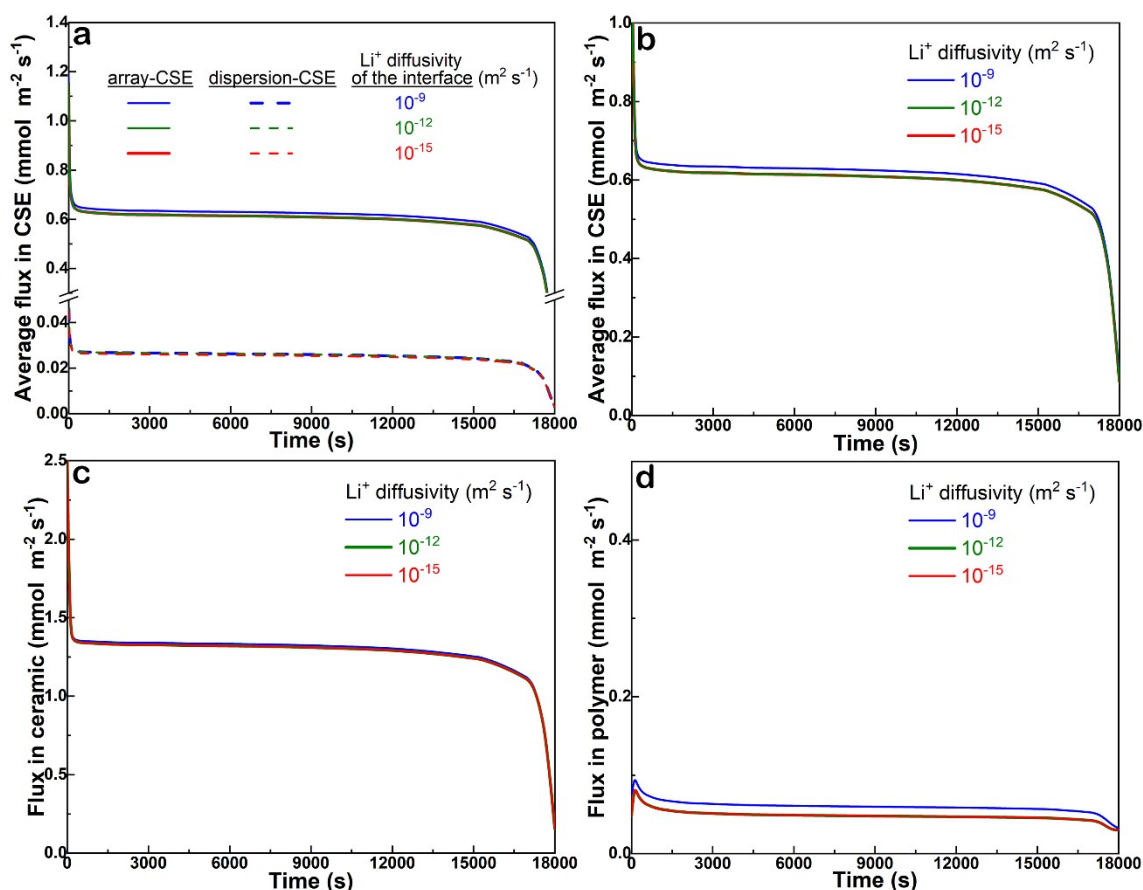
Figure S10 (a) Comparison of FEM simulations on average Li⁺ fluxes in array-CSE and dispersion-CSE with a 1-nm interface layer. FEM simulations of (b) average Li⁺ flux, (c) Li⁺ flux in the ceramic region, and (d) Li⁺ flux in the PVDF-HFP region, as a function of discharging time, in the array-CSE with a 1-nm interface layer having Li⁺ diffusivity of 10^{-15} to 10^{-9} m² s⁻¹ between LLZTO and PVDF-HFP.
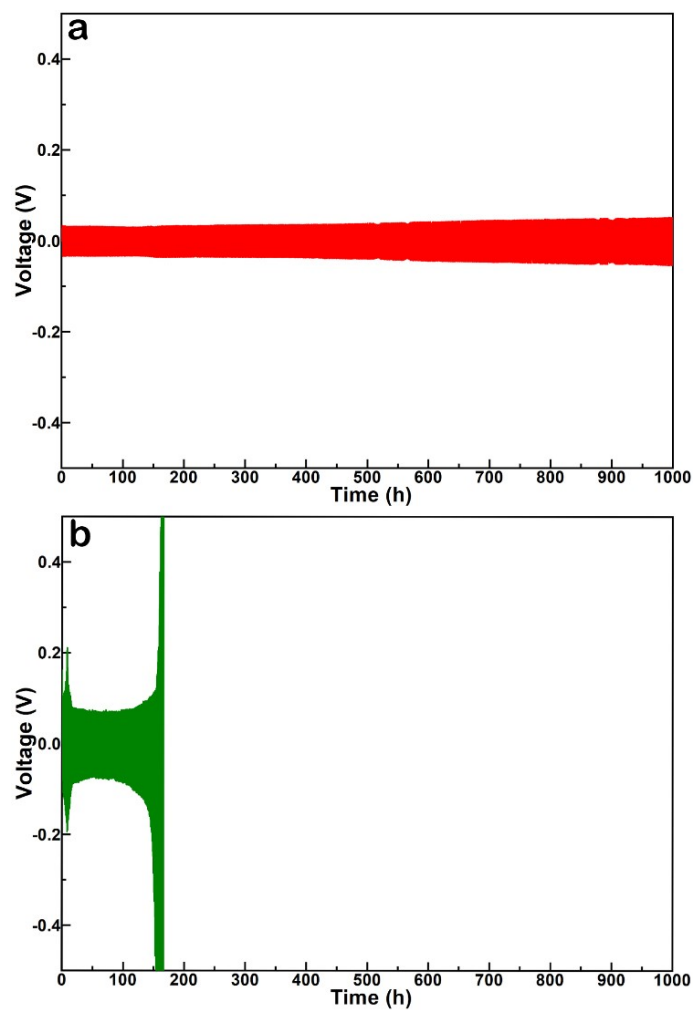
Figure S11 Plating-stripping behavior of symmetric Li|CSE|Li cells using array-CSE, comparing (a) with and (b) without the addition of the coupling agent in the fabrication process, at a constant current of 0.1 mA cm^{-2}.
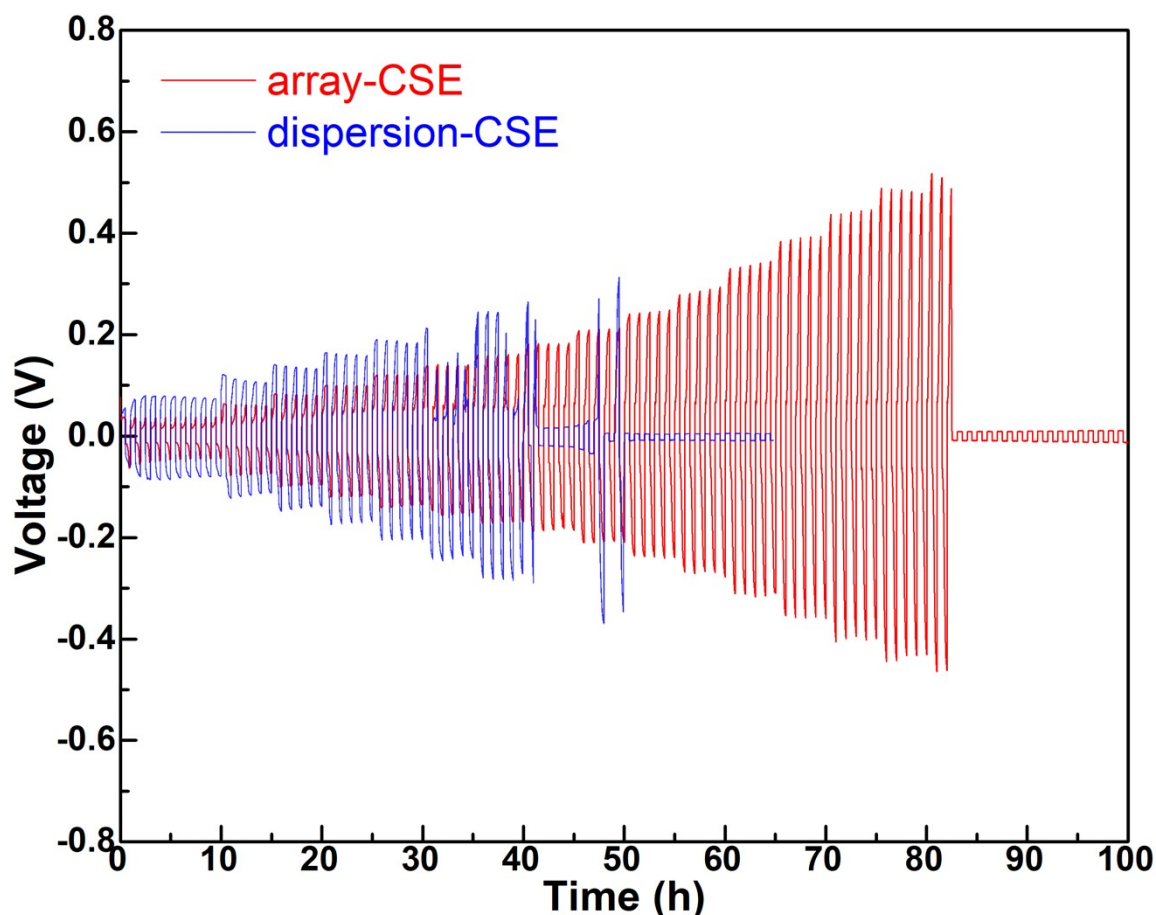
Figure S12 Plating and stripping behavior of symmetric Li|LLZTO|Li cells, conducted under varying currents, starting at 0.1 mA cm^{-2} and escalating until cell failure.

To improve the contact between the CSE and the Li anode in Figure S12 testing, a small amount of liquid electrolyte was introduced at the interface between the CSE and the Li anode. The rate capability and critical current density (CCD) of symmetric cells, using the array-CSE and dispersion-CSE as the electrolytes, were evaluated by cycling the cells with charging and discharging under varying current densities. The plating and stripping cycles were carried out at 1-h intervals until the cells failed. The first ten cycles were executed at a current density of 0.1 mA cm^{-2}, with a consistent increase of 0.12 mA cm^{-2} every five cycles during the subsequent plating-stripping process. The CCD for the cell constructed with the array-CSE was 1.90 mA cm^{-2}, while the cell assembled with the dispersion-CSE exhibited a CCD of 0.82 mA cm^{-2}. Both cells experienced failure due to short circuits.
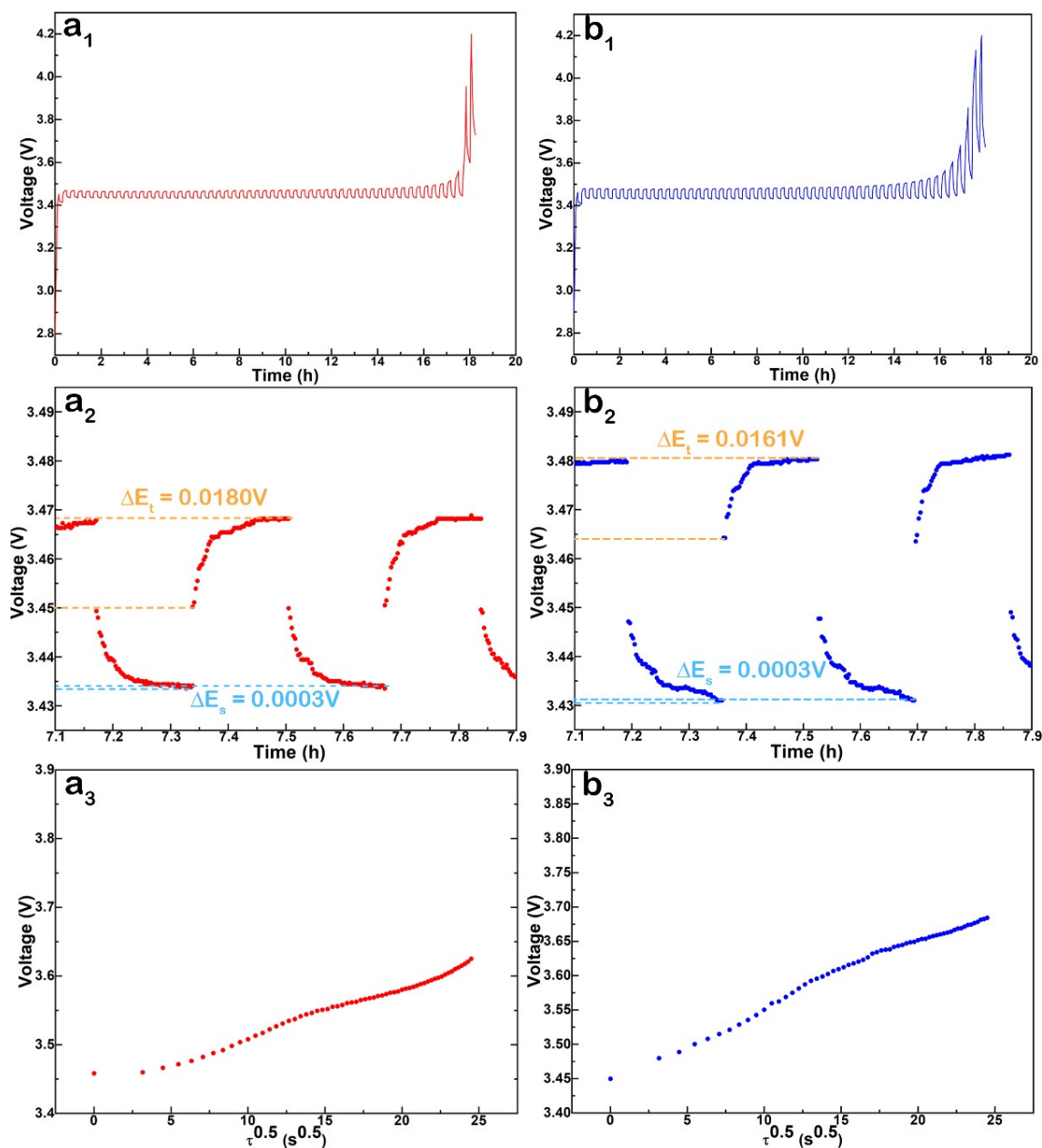
Figure S13 GITT curves of the LFP batteries with (a$_1$) array-CSE and (b$_1$) dispersion-CSE during charge stage. GITT voltage curves for the batteries with (a$_2$) array-CSE and (b$_2$) dispersion-CSE; the ΔE_t and ΔE_s values are indicated. Relationship between E(V) and $\sqrt{t}$ in GITT for the batteries with (a$_3$) array-CSE and (b$_3$) dispersion-CSE.
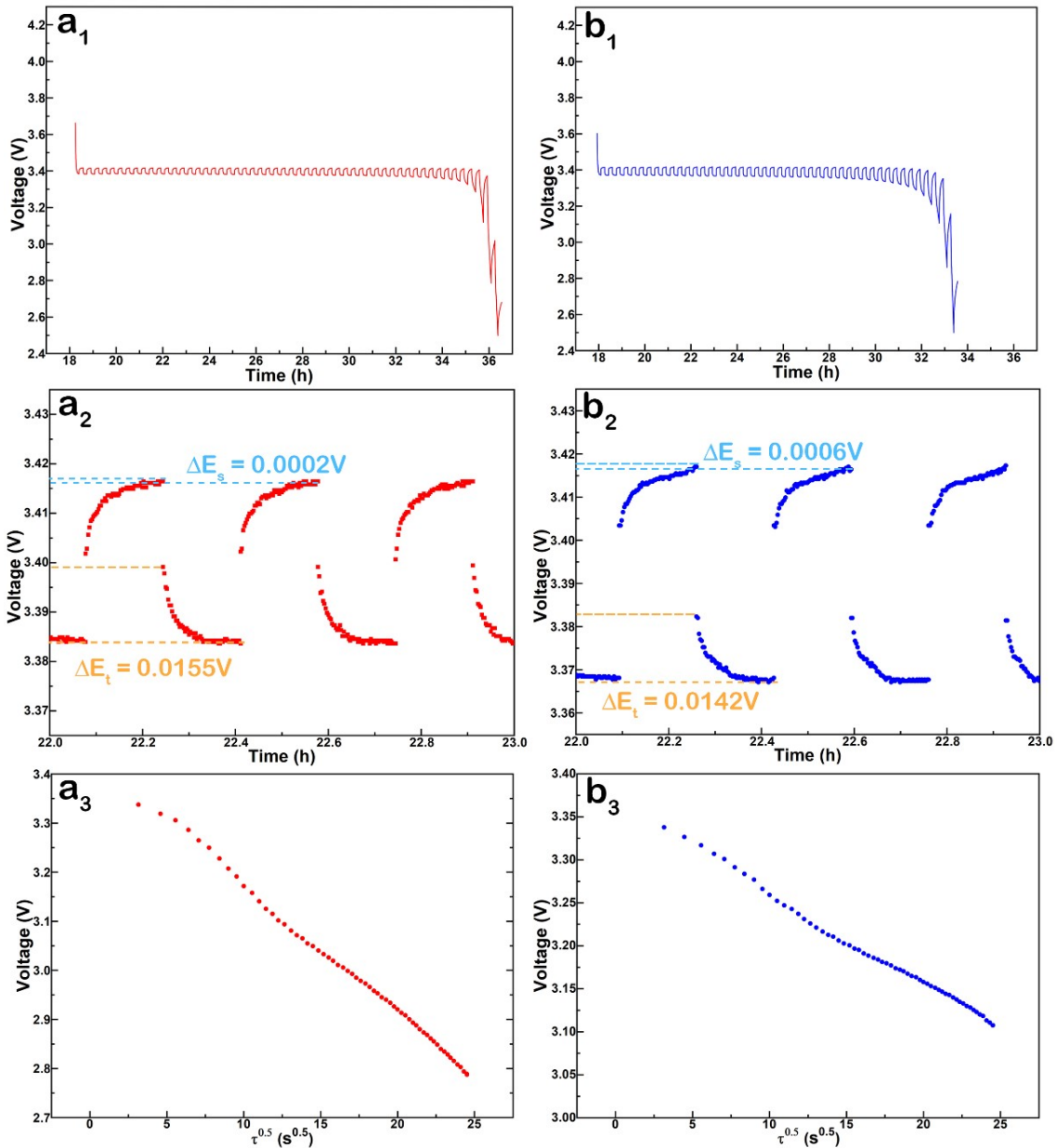
Figure S14 GITT curves of the LFP batteries with (a$_1$) array-CSE and (b$_1$) dispersion-CSE during discharge stage. GITT voltage curves for the batteries with (a$_2$) array-CSE and (b$_2$) dispersion-CSE; the ΔE_t and ΔE_s values are indicated. Relationship between E(V) and $\sqrt{t}$ in GITT for the batteries with (a$_3$) array-CSE and (b$_3$) dispersion-CSE.
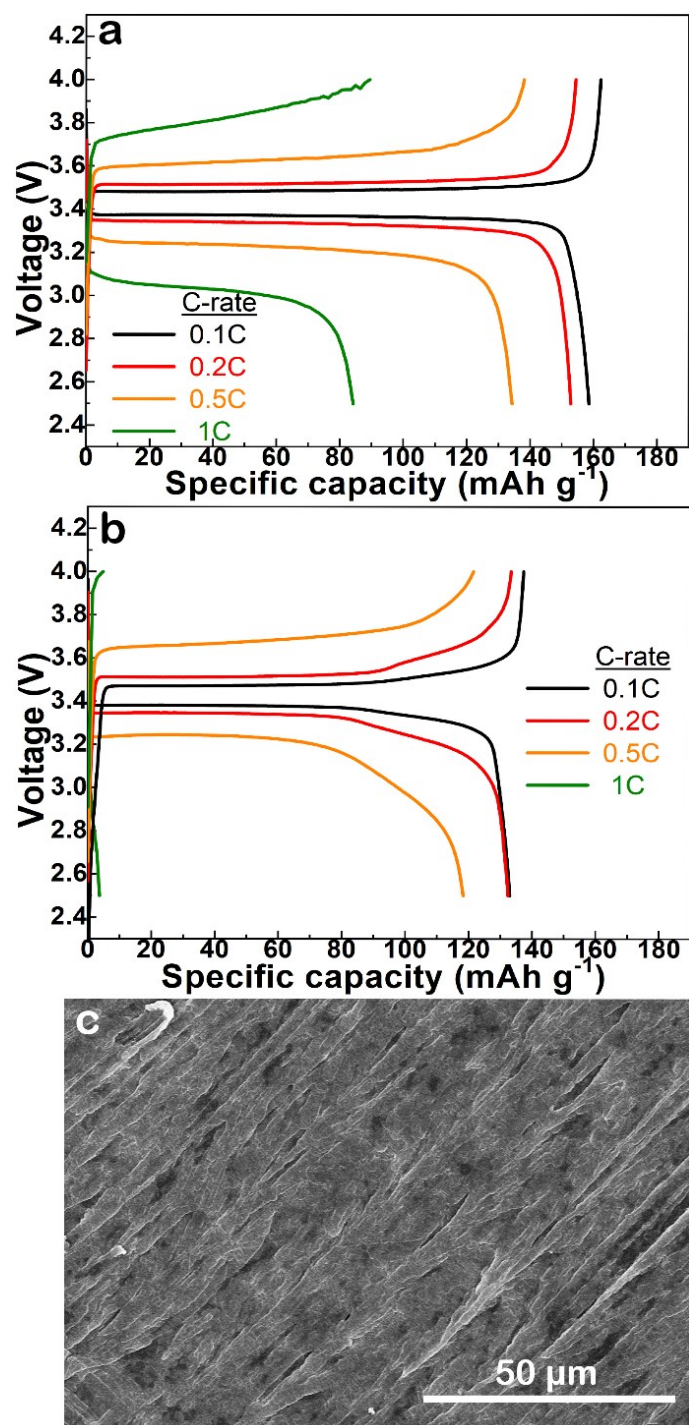
Figure S15 The charge-discharge profiles of the LFP batteries with (a) array-CSE and (b) dispersion-CSE at various C-rates. (c) Surface image of a fresh Li anode.